JOURNAL OF MATERIALS SCIENCE 24 (1989) 2369–2379

Corrosion inhibition in magnesium–aluminium-based alloys induced by rapid solidification processing

F. HEHMANN, F. SOMMER
Max-Planck-Institut für Metallforschung, Institut für Werkstoffwissenschaften, Seestrasse 75, D-7000 Stuttgart, West Germany

H. JONES, R. G. J. EDYVEAN
School of Materials, University of Sheffield, Mappin Street, Sheffield S1 3JD, UK

The effect of rapid solidification on the corrosion behaviour in aerated 0.001 M NaCl solution of Mg–Al alloys containing 9.6 to 23.4 wt% Al has been investigated in comparison with chill-cast material. Polarization studies show that rapid solidification decreases corrosion current by up to two orders of magnitude corresponding to a corrosion rate of 6 to 11 mil y^{-1}. Increasing the aluminium content in solid solution by rapid solidification gave rise to a steep increase in pitting potential between 10 and 23 wt% Al and resulted in development of an anodic plateau at $\sim 30\,\mu A\,cm^{-2}$ attributable to magnesium depletion for the alloy surface and formation of a protective film. Chemical analysis of the electrolyte as a function of dissolution time for the rapidly solidified material indicated that initially only magnesium dissolved and that this dissolution of magnesium ceased within 2 to 5 min. The results indicate the formation of an aluminium-enriched interdiffusion zone at the surface underlying a more stable surface oxide than for ingot-processed Mg–Al-based alloys.

1. Introduction

Although magnesium and aluminium have similar negative galvanic potentials, aluminium readily exhibits corrosion resistance as a result of the formation of a self-healing passive alumina-based protective film [1]. Magnesium and its alloys in contrast tend to form an $Mg(OH)_2$ or derived film that is nonprotective in environments containing anions such as Cl^-, CO_3^{2-} or SO_4^{2-} giving pH values less than 10, as for example under common atmospheric conditions [1–4]. Rapid solidification processing offers the opportunity to extend solid solubility, produce novel phases and refine and homogenize microstructure, all of which could contribute towards formation of protective surface films and elimination of micro-galvanic effects [5]. This has been demonstrated [6–8] in recent work by Allied Signal in which extended alloying made possible by rapid solidification processing was reported to result in exceptionally low corrosion rates in 3 wt% NaCl solution (e.g. 11 mil y^{-1} ($\sim 279\,\mu m\,y^{-1}$) for extrusions of melt-spun Mg–5 wt% Al–7 wt% Y–5 wt% Zn compared with ~ 63 mil y^{-1} ($\sim 1600\,\mu m\,y^{-1}$) for the most corrosion resistant ingot-processed magnesium alloy AZ91 HP = Mg–9 wt% Al–1 wt% Zn).

The present work forms part of a systematic investigation of the effect of rapid solidification on the corrosion behaviour of magnesium alloys containing selected binary additions. A previous paper has described the effect of representative additions to magnesium of aluminium, manganese, yttrium and selected lanthanides on the corrosion behaviour of melt-spun and splat-cooled samples in chloride-free and chloride-doped aqueous environments [9]. The present paper reports more detailed investigations for Mg–Al alloys over a wide range of composition (9.6 to 62.3 wt % Al) in the chill-cast, splat-cooled and melt-spun conditions.

2. Experimental procedure

Mg–Al alloys containing 9.6, 16.0, 17.6, 19.4, 23.4 and 62.3 wt % Al were made from magnesium of two different purities (99.95 wt % Mg with 0.032 ± 0.003 wt % Fe, 0.004 ± 0.002 wt % Mn, < 0.01 wt % Si, < 0.005 wt % Al and < 0.0005 wt % Cu and 99.5 wt % Mg with 0.12 ± 0.02 wt % Si, 0.072 ± 0.015 wt % Al, 0.014 ± 0.005 wt % Fe, 0.005 ± 0.001 wt % Mn and < 0.0005 wt % Cu) and aluminium of 99.999 wt % purity. Melting was carried out under argon in MgO crucibles to produce chill-cast slabs of thickness 7 mm. Piston-and-anvil splat cooling was performed in an argon atmosphere; melt spinning was done in a helium atmosphere. Splat quenching gave specimens of thickness 110 to 130 μm. For melt spinning, a copper wheel 300 mm in diameter and surface finish 1 μm was used. By employing a wheel speed of 4200 r.p.m., a crucible gas pressure of 250 mbar, a crucible nozzle of ~ 1.0 mm, a distance between nozzle and wheel of 2.25 mm and an angle between crucible and off-centre line of 3°, the resulting ribbons were $\sim 30\,\mu m$ thick and 1.8 to 2.0 mm wide.

Two methods of electrochemical characterization were employed:

1. potentiodynamic polarization using sweep rates of 2 or 6 mV sec^{-1} in the range of -3 V to $+3$ V with respect to the free corrosion potential of the alloy concerned;
2. potentiostatic anodic polarization in conjunction with chemical analysis of the electrolyte as a function of time of electrolysis.

The experimental conditions employed for potentiodynamic polarization are summarized in Table I. The long cathodic sweep as applied particularly to heat-treated samples or to samples that had been exposed to normal atmosphere for several months was aimed at removing surface films prior to the electrolysis. Aerated 0.001 M NaCl aqueous solution gave an effective pH value of 4.9 $\pm$ 0.1 (allowing the formation of passive alumina-based surface films) and distilled water gave an effective pH-value of 5.8 $\pm$ 0.2, owing to the presence of Cl^- ions and/or CO_2, O_2 and other species picked up from the atmosphere. The acidity of the electrolyte plus the presence of Cl^-, O^{2-} and other anions should have ensured that any anodic polarization observed did not stem from the films formed in humid air, but from enhanced alloying by rapid solidification processing (RSP). Under these conditions the anodic dissolution was not inhibited and started spontaneously for all alloys investigated. Subsequent polarization effects where observed increased with increasing sweep rate. The long anodic sweep should verify any possibility of novel surface films with a protective character. Because the degree of microstructural and chemical refinement and of quenched-in vacancies and other defects affects both pitting and corrosion potentials, the effect of RSP on the corrodability of a given alloy is better accounted for by the differences between pitting and corrosion potential, which is called "anodic polarization" in this paper, rather than by the absolute values of the pitting potentials. After completion of the first scan the pH value of the electrolyte of volume 200 ml amounted to $\sim$8.0, after the second to $\sim$9.6. During the potentiodynamic and potentiostatic scans the electrolyte was stirred with a plastic-coated magnetic stirring bar. The cell design consisted of a standard calomel reference electrode fitted into a potassium chloride saturated agar Haber–Luggin capillary salt bridge. In order to ensure a reproducible and undisturbed cell current the orifice of the Haber–Luggin capillary was adjusted to the centre of the sample and the distance between the orifice and the sample did not exceed 1 mm. Reproducibility of the experiments was achieved by employing a fixed surface geometry of small surface area. The actual surface area of the samples ranged from 0.6 to 1.0 cm^2. A cylindrical platinum grid of 50 mesh and of internal diameter 45 mm was used as the auxiliary electrode. The experiments were performed by using a software controlled "Autostat" manufactured by Thomson Electrochem. Ltd. Samples were cleaned with alcohol and dilute acid and those surfaces not to be investigated were then treated with "lacomit". In order to ensure a good bond between metal and lacomit coating the lacomit was left at room temperature for at least 24 h so as to dry out completely. Chemical analysis of the electrolyte was done by flame (for magnesium) and flameless (aluminium) atomic absorption analysis.

3. Results

3.1. Microstructures

Fig. 1 shows representative optical microstructure of the samples investigated. Splat samples were taken from the central portion of the piston-and-anvil splats. The Mg–9.6 wt % Al splat investigated showed essentially a rosetted two-phase microstructure between columnar chill zones of width 15 to 20 μm (Fig. 1a). The Mg–16.0 wt % Al splats were characterized by a featureless chill zone of thickness $\sim$40 μm at the side of second impact of the piston succeeded by a columnar-dendritic zone and then by an equiaxed two-phase microstructure (Figs 1b,c). The Mg–Al alloy ribbons exhibited essentially featureless columnar growth over the entire cross-section of thickness 25 to 30 μm (Figs 1d to f). Only the ribbon with 17.6 wt % Al occasionally showed some microcellular microstructure at the wheel off-side of the ribbon (Fig. 1d). Transmission electron microscopy on $\sim$30 μm thick ribbon samples containing 21.6 at % Al showed an essentially single-phase solidification structure with intragranular microcells of size 0.01 to 0.40 μm. After 7 mon room temperature ageing, an ordered coherent phase of size $\sim$5 nm and of unknown composition was observed in Mg–21.6 at % Al ribbon preferentially occurring at low-angle boundaries (Fig. 1f) [10]. The corrosion studies on the ribbons (splats) have been performed after 2 to 2.5 (9) mon room-temperature ageing. The microstructure of the chill-cast slabs consisted of α-dendrites with a volume fraction of interdendritic eutectic network that increased with increasing aluminium concentration (Figs 1h to k). Chill-cast Mg–62.3 wt % Al was virtually single-phase (β-Al_8Mg_5) with some interdendritic eutectic (Fig. 1g).

TABLE I Conditions employed for potentiodynamic polarization on splat-cooled, melt-spun and chill-cast Mg-Al alloys and extrusions of Mg–Al–Zn–Y (Allied)

Electrolyte (200 ml)	aerated pH = 4.9 $\pm$ 0.1/0.001 M NaCl aqueous solution
Temperature of electrolyte (° C)	20 $\pm$ 2
Sweep range (V)	from -3 to $+3$ V with respect to the free corrosion potential
Sweep rate (mV sec^{-1})	ribbons: 6 splats: 2(from -3 to -1 V), extrusions: 6
Surface conditions:	
splats	as-splatted on 1000 grit finished Cu–1.5 wt % Be
ribbons	as-spun on 1 μm finished copper wheel
chill-cast material and extrusions	1 μm polished surface

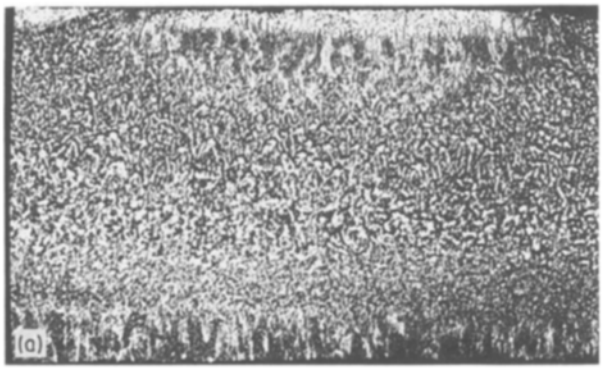

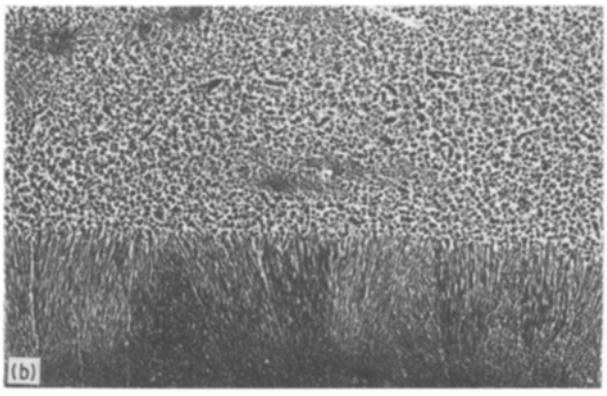

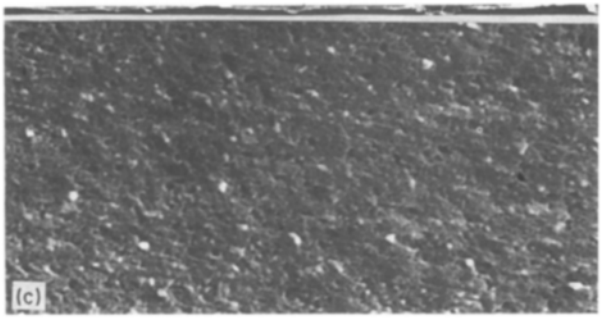

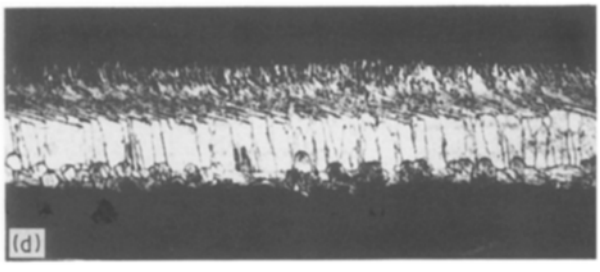

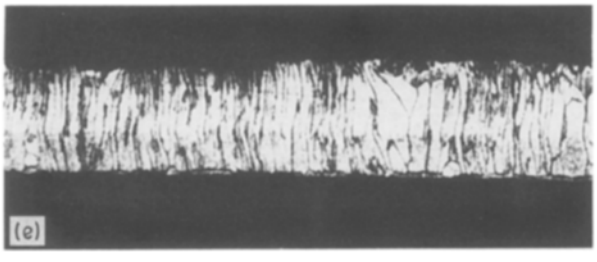

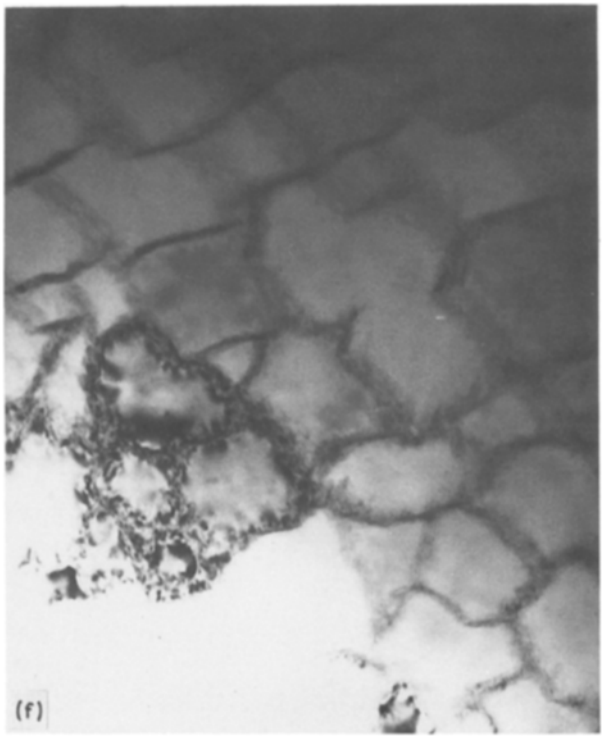

Figure 1 Representative microstructures of transverse sections of single-phase and two-phase Mg–Al alloys, optical, if not indicated otherwise, with concentration in wt %. Chemically etched in 0.1 nital. (a) Piston-and-anvil splat with 9.6 Al, × 340. (b) Piston-and-anvil splat with 16.0 Al, SEM, × 640. (c) Magnified section of single-phase chill zone of (b), SEM, × 6800. (d) As-spun ribbon with 17.6 Al, × 700. (e) As-spun ribbon with 23.4 Al, × 700. (f) as (e), here in transgranular microcells, TEM, × 42 000. (g) Chill-cast slab with 62.3 Al, × 638. (h) Chill-cast slab with 9.6 Al, × 660. (i) Chill-cast slab with 17.6 Al, × 660. (j) Chill-cast slab with 19.4 Al, × 660. (k) Chill-cast slab with 23.4 Al, × 660. (a, b) Side of second impact down with chill zone of between 15 to 40 μm. The splats displayed a small second chill zone on the side of first impact of the pistons (top). (d, e) Recalesced chill-side down.

3.2. Potentiodynamic polarization behaviour

The results of electrochemical tests are summarized in Table II.

3.2.1. Effect of rapid solidification

Fig. 2 shows the improved corrosion behaviour of the recalesced chill-zone of an Mg–9.6 wt % Al splat compared with the corresponding chill-cast material. The reduction in corrosion current amounts to approximately one order of magnitude. This improvement increases to two orders of magnitude for the ribbons with 17.6 and more wt % Al (Fig. 3). The free corrosion potential of the rapidly solidified compared to the chill-cast material decreased by ~300 to ~600 mV (see Table II). It is interesting to note the frequent observation that the free surface of the ribbons showed higher pitting potentials than the corresponding wheel-on side while at low anodic polarization the anodic dissolution and hence the corrosion current was stronger for the free than for the chill side (see Table II and Fig. 4).

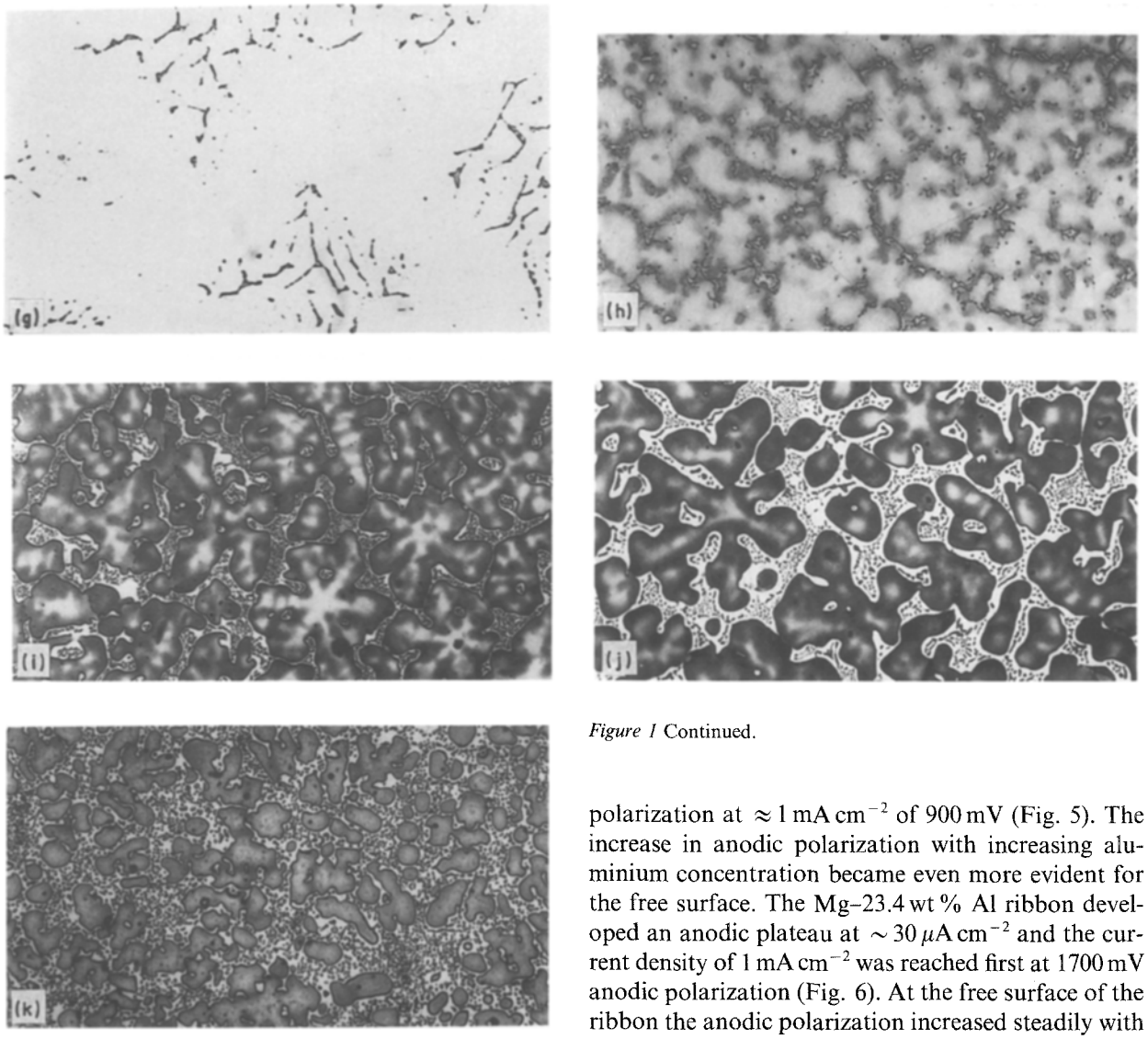

Figure 1 Continued.

3.2.2. Effect of aluminium content

An increase in alloying content from 9.6 to 23.4 wt % Al in the recalesced chill-zone of rapidly solidified samples gave a decrease in corrosion current of about two orders of magnitude and an increase in anodic polarization at $\approx 1\,mA\,cm^{-2}$ of 900 mV (Fig. 5). The increase in anodic polarization with increasing aluminium concentration became even more evident for the free surface. The Mg–23.4 wt % Al ribbon developed an anodic plateau at $\sim 30\,\mu A\,cm^{-2}$ and the current density of $1\,mA\,cm^{-2}$ was reached first at 1700 mV anodic polarization (Fig. 6). At the free surface of the ribbon the anodic polarization increased steadily with aluminium concentration (Fig. 6), whereas the chill side of the ribbon did not show such a clear relationship (see Table II). Chill-cast Mg–62.3 wt % Al (see Fig. 1g), finally, displayed a pitting potential of +2500 mV resulting in a large anodic plateau and an anodic polarization of 3200 mV, while the corrosion current

TABLE II Results from potentiodynamic polarization of Mg–Al alloys in aerated pH = 4.9 ± 0.1 0.001 M NaCl aqueous solution using a sweep rate of 6 mV sec^{-1}

Alloy concentration (wt %)	Chill-cast material ($\sim 10^3$ K sec^{-1})				Rapidly solidified material ($\sim 10^5$ to $> 10^6$ K sec^{-1})							
					Recalesced chill-zone				Two-phase or free surface			
	I_c ($\mu A\,cm^{-2}$)	W (mil y^{-1})	E_c	π (V)	I_c ($\mu A\,cm^{-2}$)	W (mil y^{-1})	E_c	π (V)	I_c ($\mu A\,cm^{-2}$)	W (mil y^{-1})	E_c	π (V)
Piston-and-anvil splats												
9.6	2900	2610	−0.45	0.18	100–200	89.0–198	−0.8	0.26	950	855	−0.8	0.02
16.0	1000	900	−0.35	–	9.0–13.0	8.1– 11.7	−1.3	0.50	270	243	−0.45	0.30
Melt-spun ribbon												
17.6	250–950	225–855	−0.7	0.03	12.0	10.8	−1.2	1.61	24–40	21.6–36.0	−1.3	0.74
19.4	580	522	−0.65	0.61	8.0	7.20	−0.8	0.96	35	31.5	−1.25	1.00
23.4	480–670	432–603	−0.7	0.14	6.5	5.85	−1.1	1.02	28	25.2	−1.3	1.70
62.5	80	72	−1.2	3.20								

I_c: corrosion current.

W: annual corrosion rate (1 mil = 10^{-3} in. $W = \dfrac{A(g\,mol^{-1})\,I_c(mA\,cm^{-2})}{zF(mA\,sec\,mol^{-1})(g\,cm^{-3})}\,t\,\dfrac{10^3\,mil}{2.54\,cm}$

where $t = 31.536 \times 10^6\,sec\,y^{-1}$, z = valency of dissolving component (Mg = 2), A = atomic weight of dissolving component, ϱ = density of dissolving component, I_c = corrosion current observed, F = Faraday's constant.

E_c: corrosion potential.

π: anodic polarization = corrosion potential minus pitting potential here at a current density of $1\,mA\,cm^{-2}$.

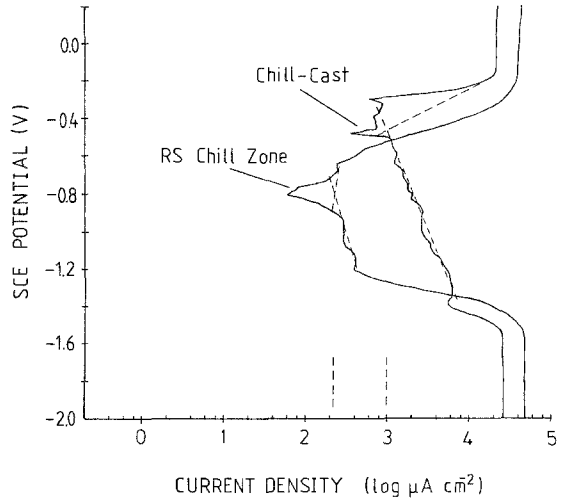

Figure 2 Potentiodynamic polarization against corrosion current in aerated 0.001 M NaCl aqueous solution of pH = 4.9 ± 0.1 at 20 ± 2° C using a sweep rate of 6 mV sec^{-1} for chill zone (second impact) of as-splatted Mg–9.6 wt % Al piston-and-anvil splat and of chill-cast Mg–9.6 wt % Al. SCE: standard calomel electrode.

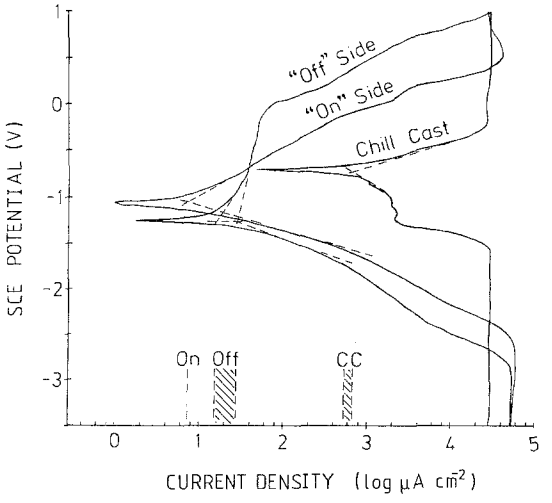

Figure 4 Potentiodynamic polarization of the wheel-on and the wheel-off side of as-spun Mg–23.4 wt % Al and of chill-cast Mg–23.4 wt % Al. Experimental conditions as for Fig. 2.

did not reduce compared to the ribbons (Table II). The corrosion current and the anodic polarization of the coarsely segregated chill-cast magnesium-based samples with 9.6 to 23.4 wt % Al was found to be independent of aluminium concentration (Table II).

3.2.3. Further observations

Fig. 7 shows scans 1 and 2 on the wheel-on side of as-spun Mg–23.4 wt % Al. Because the pH value during scan 1 changed from 4.9 to ~ 8 and during scan 2 from ~ 8 to 9.6, the reduced anodic current density indicated by the hatched area may stem from both the depletion of magnesium from the surface and the pH value of 8 to 9.6 making the electrolyte less aggressive.

Three basic observations were made during potentiodynamic polarization, however, which support the depletion hypothesis.

1. The difference in current density between scans 1 and 2 decreased with increasing aluminium concentration for a given microstructure and sample area.
2. The difference between scans 1 and 2 increased with increasing homogeneity as indicated by the microstructure for a given concentration.
3. Scan 2 of the ribbon increasingly resembled scan 1 of chill-cast Mg–62.3 wt % Al the higher the aluminium concentration.

Fig. 8 shows the polarization curve for a sample of as-extruded PM-Mg–5 wt % Al–5 wt % Zn–7 wt % Y supplied by Allied and for as-spun Mg–23.4 wt % Al. It indicates no significant difference in corrosion behaviour, i.e. corrosion current, anodic polarization and the overall shape of the potentiodynamic curve, between these two materials. Although the alloys do not show true passivation, anodic polarization was observed with steadily increasing current density, the corresponding Tafel-slope $(d\varepsilon)/d(\log I)$ being ~ 0.5. It is notable that 23.4 wt % Al confers the same improvement in corrosion resistance of magnesium under conditions of rapid solidifications as the three solutes do in extrusions of rapidly solidified Mg–5Al–5Zn–7Y (wt %). Beyond the pitting potential, the ribbon developed an apparently uniform tarnish, while the Allied material showed local pitting. Samples of extrusions of rapidly solidified Mg–5Al–2Zn–1Nd

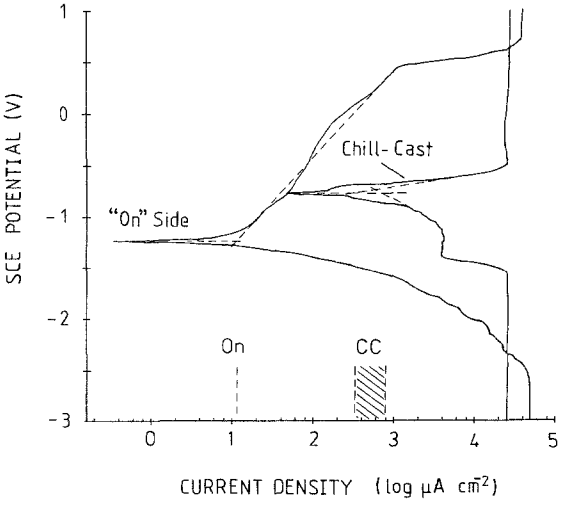

Figure 3 Potentiodynamic polarization of the wheel-on side of Mg–17.6 wt % Al ribbon and of the corresponding chill-cast material. Experimental conditions as for Fig. 2.

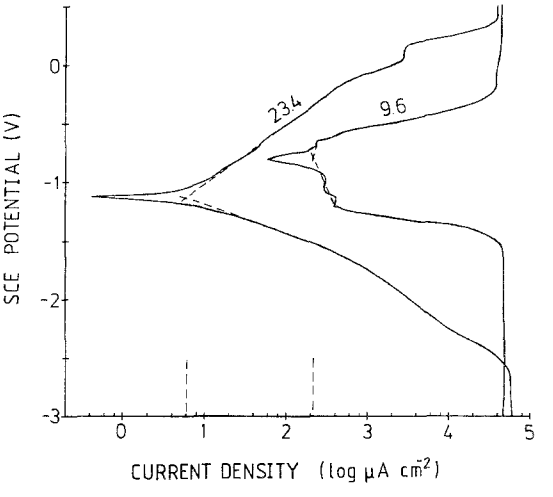

Figure 5 Potentiodynamic polarization of the chill zones of as-splatted Mg–9.6 wt % Al piston-and-anvil splat and of as-spun Mg–23.4 wt % Al ribbon. Experimental conditions as for Fig. 2.

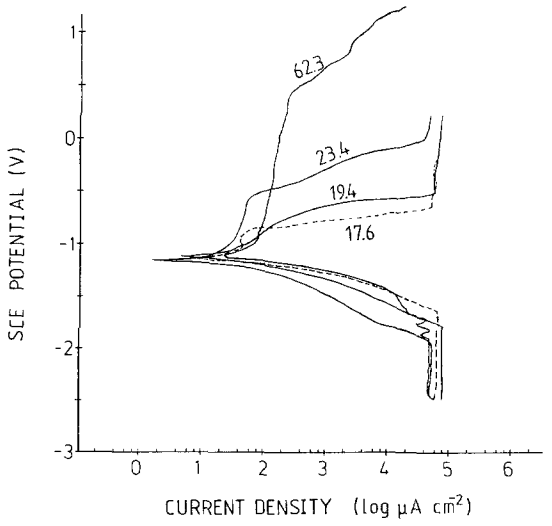

Figure 6 Potentiodynamic polarization of the chill zone of as-splatted Mg–9.6 wt % Al, of the wheel-off side of as-spun Mg–Al ribbon containing 17.6, 19.4 and 23.4 wt % Al and of chill-cast 62.3 wt % Al showing increasing anodic polarization (pitting potential) with increasing aluminium content. Experimental conditions as for Fig. 2.

supplied by Allied, exhibited higher corrosion currents and lower pitting potential than their Mg–5Al–7Y–5Zn (wt %).

3.3. Potentiostatic polarization behaviour

Potentiostatic sweeps were employed to allow measurement of the rate of dissolution of magnesium and aluminium from as-spun and chill-cast Mg–Al alloys by chemical analysis of the electrolyte as a function of dissolution. Fig. 9 shows current density plotted against potentiostatic polarization time for Mg–23.4 at % Al ribbon and corresponding chill-cast material anodically polarized at + 150 mV. After rapid initial dissolution the current decreases to an unsteady low current density regime between 4 and 10 min followed by a second peak and they by a second low current density regime before the immersed part of the ribbon broke off after 16 min 20 sec due to aerated cells along the line where the uncoated surface of the ribbon passes through the electrolyte/air interface. In contrast, the chill-cast

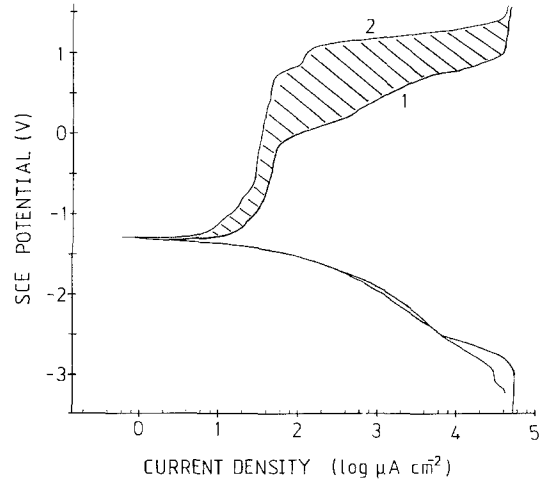

Figure 7 Scans 1 and 2 of potentiodynamic polarization of the wheel-off side of as-spun Mg–23.4 wt % Al ribbon reflecting depletion of the ribbon surface of magnesium atoms. Experimental conditions as for Fig. 2.

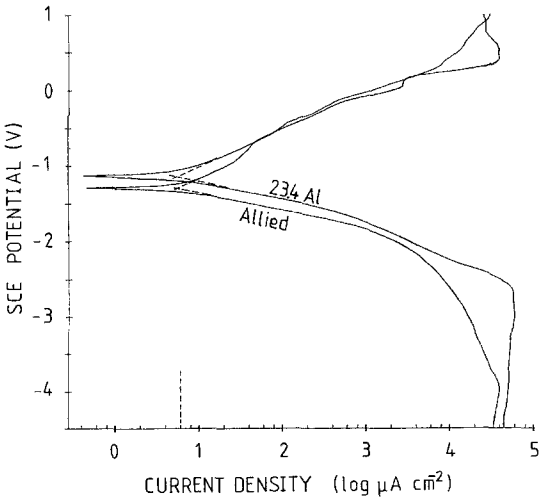

Figure 8 Potentiodynamic polarization of as-spun Mg-23.4 wt % Al ribbon and of Allied as-extruded Mg–5 Al–5 Zn–7 Y (wt %) and showing similar corrosion behaviour. Experimental conditions as for Fig. 2.

Mg–23.4 wt % Al alloy showed essentially constant current density in the high current density regime over the entire 30 min of electrolysis.

3.3.1. Magnesium dissolution

The sudden increase in current density of the ribbon after ~ 1 and 10 min electrolysis time (Fig. 9) corresponds to the two increases in magnesium dissolution from the ribbon shown in Fig. 10a, while the constant current density for the chill-cast material corresponds to the constant magnesium dissolution rate shown in Fig. 10a. The difference between chill-cast and rapidly solidified material became more obvious when applying an anodic polarization of 1900 mV (Fig. 10b). Figs 11a and b summarize the results of magnesium analysis of the electrolytes for as-spun and chill-cast Mg–23.4 wt % Al alloy as a function of duration of anodic polarization. Whilst all ribbon samples exhibited initially an exponential decrease in dissolution rate followed by a virtual cessation of magnesium dissolution after ~ 5 min polarization, the chill-cast samples showed continuous and up to one order of magnitude higher dissolution rates for magnesium. The virtual stopping of magnesium dissolution after ~ 5 min was relatively independent of the potential employed. The surface of the rapidly solidified Mg–Al samples remained untarnished during the time of inactive magnesium dissolution, while the chill-cast material built up a greyish, salt-like layer at polarizations ⩾ 150 mV. Piston-and anvil splats containing 16.0 wt % Al were inactive when anodically polarized at 150 mV, but they showed essentially the same behaviour as chill-cast Mg–23.4 wt % Al when polarized at 300 or 400 mV (Fig. 12).

3.3.2. Aluminium dissolution

During the first 10 min electrolysis of as-spun Mg–23.4 wt % Al polarized at ~ 1900 mV, the aluminium content of the electrolyte did not change detectably. Above 30 min, i.e. when the second increase in magnesium concentration was observed (see Fig. 11a), the aluminium content of the electrolyte increased

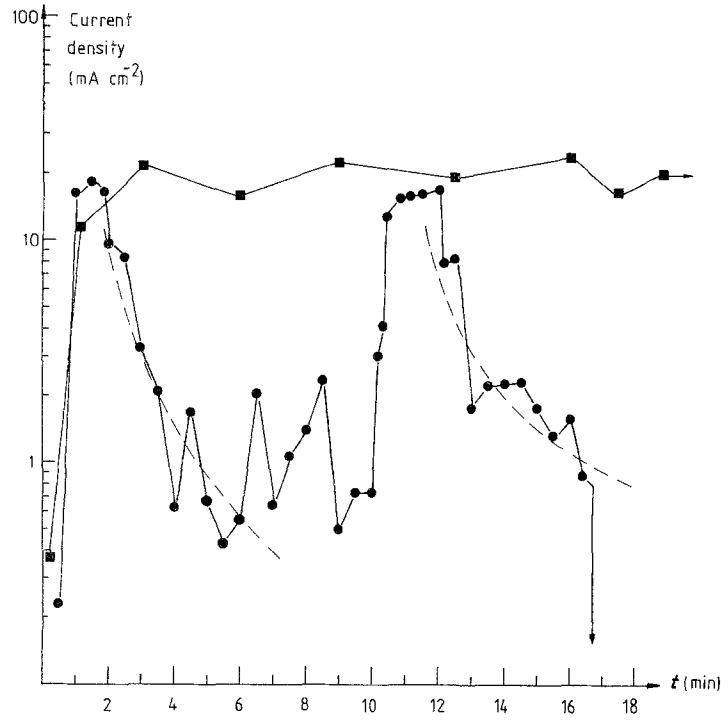

Figure 9 Current density plotted against potentiostatic polarization time of (■) chill-cast and (●) melt-spun Mg–23.4 wt % Al anodically polarized at 150 mV above the free corrosion potential. After 16 : 20 min the lower part of the ribbon broke off due to aerated cells causing localized pitting at the electrolyte/air interface at the uncoated metallic surface of the sample. (– – –) Possible $I = fn(t)^{-1/2}$ relationship (see Equation 3). Further experimental conditions as for Fig. 2.

significantly. The macroscopic aluminium loss from the sample was estimated to increase from 0.3 $\mu g\,cm^{-2}$ after 1 min electrolysis to $\sim 20\,\mu m\,cm^{-2}$ after 30 min anodic polarization. In contrast to the rapidly solidified alloys, the aluminium content of the electrolyte for chill-cast Mg–23.4 wt % Al amounted to 22 $\mu g\,cm^{-2}$ after 1 min anodic polarization. Above 1 min electrolysis, the aluminium content scattered between 35 and 150 $\mu g\,cm^{-2}$ without showing any trend. This may indicate major re-deposition of aluminium atoms on the surface by participating in the formation of the salt-like layer observed.

3.3.3. Selectivity

After 1 min anodic polarization at ~ 1900 mV with respect to the free corrosion potential, the dissolution rates, dc/dt, of the Mg–23.4 wt % Al alloy amounted to 613 $\mu g\,cm^{-2}\,min^{-1}$ Mg and $\sim 20\,\mu g\,cm^{-2}\,min^{-1}$ Al for the chill-cast material; 49 $\mu g\,cm^{-2}\,min^{-1}$ Mg and $\approx 0.3\,\mu g\,cm^{-2}\,min^{-1}$ Al for the as-spun ribbon. Note that the concentration of Mg^{2+} and Al^{3+} ions in the electrolyte did not significantly change between 1 and 30 min potentiostatic electrolysis of the Mg–23.4 wt % Al ribbon. The mole ratio of magnesium-to-aluminium dissolution after 1 min was 31 : 1 for the chill-cast

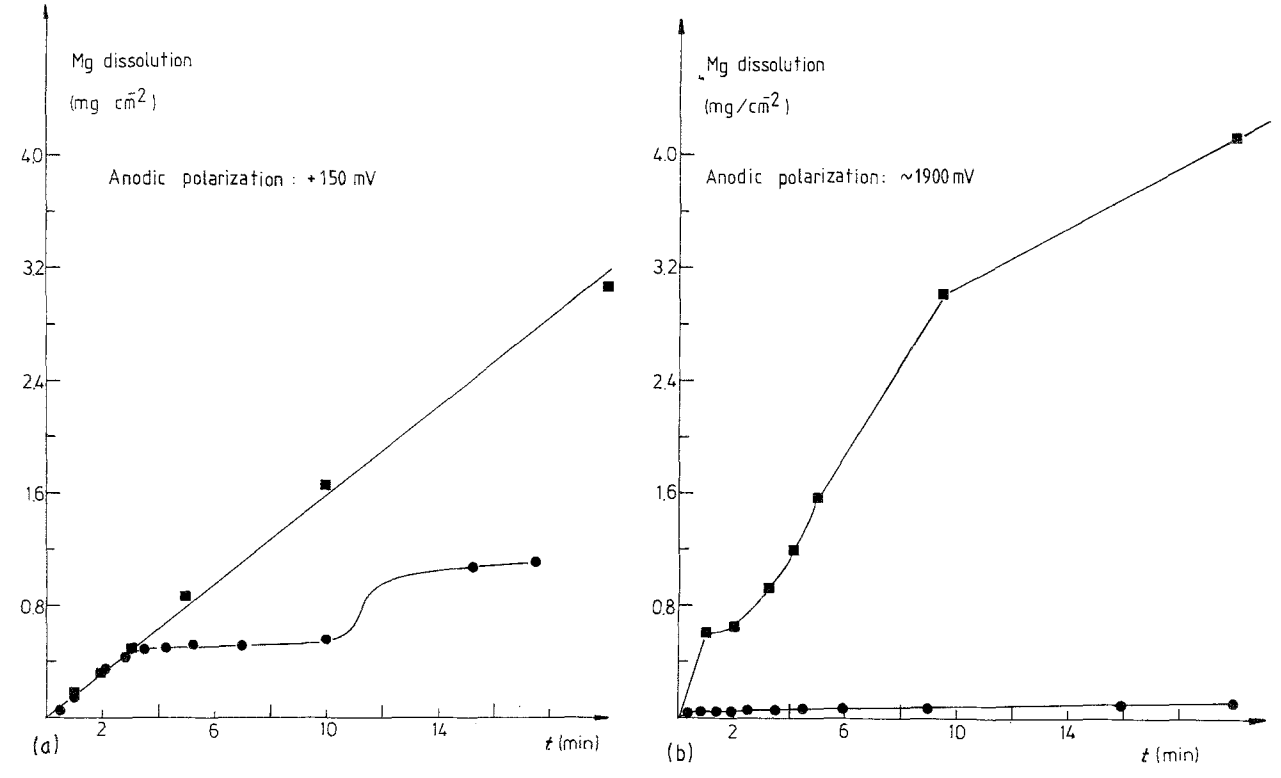

Figure 10 Magnesium dissolution rate of (■) chill-cast and (●) as-spun Mg–23.4 wt % Al anodically polarized at (a) 150 mV and (b) 1900 mV above the free corrosion potential. Further experimental conditions as for Fig. 2.

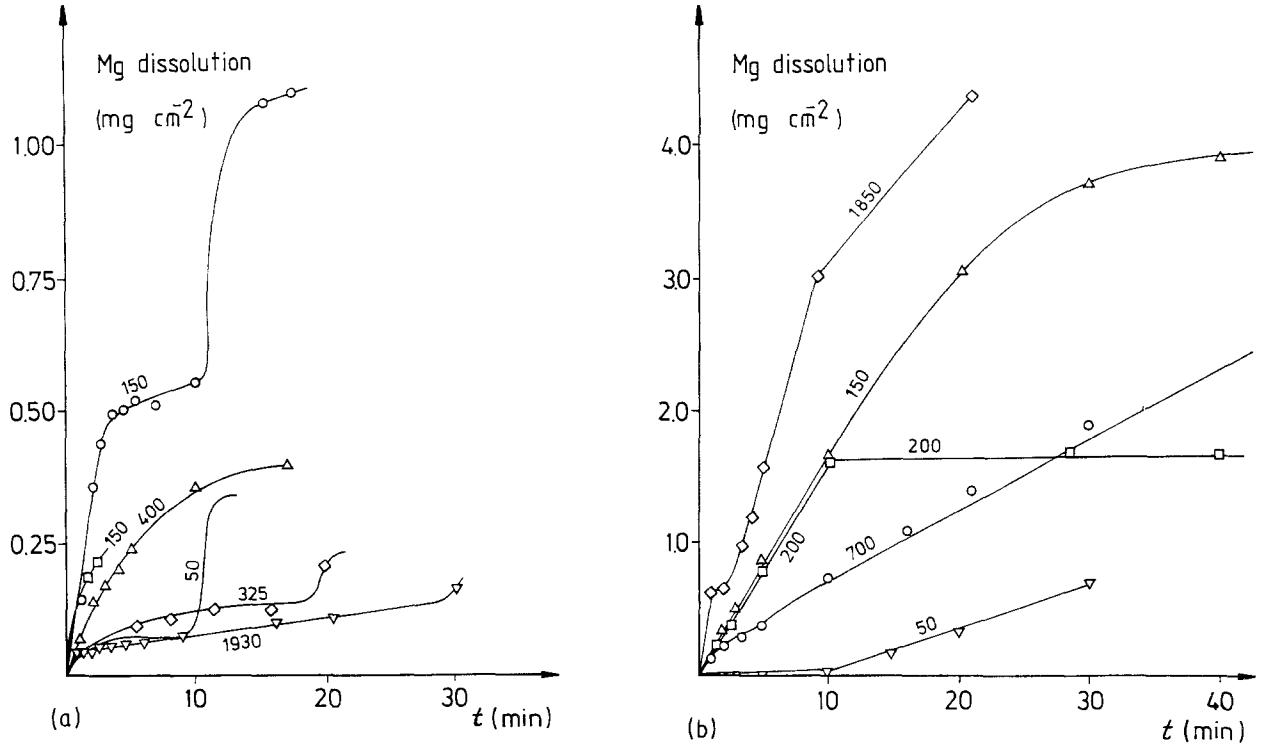

Figure 11 Magnesium loss per cm^2 against duration of potentiostatic polarization for (a) as-spun and (b) chill-cast Mg–23.4 wt % Al for various anodic polarizations above the free corrosion potential as indicated for each sample. Note the difference between (a) and (b) in the scale of the ordinate. Further experimental conditions as for Fig. 2.

material and 185 : 1 for the ribbon. The corresponding selectivity coefficient [11],

$$z = \frac{(dc/dt)_{Mg} x_{Al}}{(dc/dt)_{Al} x_{Mg}} \quad (1)$$

where dc/dt is the change of the electrolyte with time and x is the concentration of the components in the alloy (at %), after 1 min anodic polarization increased from 8.6 for the chill-cast material to 51 for the ribbon.

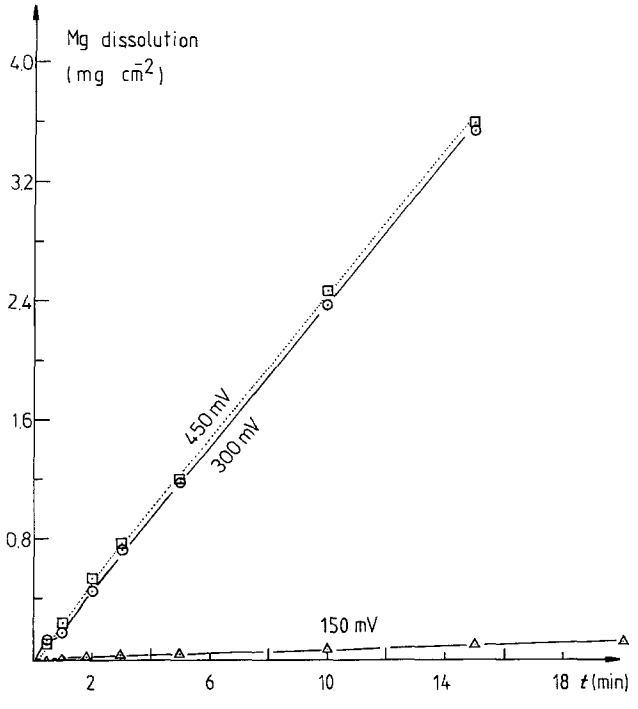

Figure 12 Dissolution rate of magnesium from chill zone of Mg–16.0 wt % Al piston-and-anvil splat polarized as indicated above the free corrosion potential. Further experimental conditions as for Fig. 2.

4. Discussion

4.1. Suppressed microgalvanic couples compared to vacancy-enhanced corrosion

The observation that the corrosion behaviour of the coarsely segregated chill-cast material is independent of aluminium concentration (Table II) confirms previous work in which corrosion of Mg–Al-based alloys was reported to occur predominantly by galvanic action between the magnesium matrix and $Mg_{17}Al_{12}$ precipitates [2, 10]. Therefore, the decrease in the anodic corrosion before pitting (or breakthrough) obtained by rapid solidification is partly due to the suppression of $Mg_{17}Al_{12}$ segregates or $Mg_{17}Al_{12}$-containing eutectic in the rapidly solidified alloys. This eliminates the operation of microgalvanic coupling between the two phases. Despite the enoblement of the matrix due to the increase in the number of microcathodic inclusions via the extension of the solid solution of aluminium in magnesium (compare [13]), however, the rapidly solidified material showed lower free corrosion potentials than the chill-cast material. This observation might result from a high quenched-in vacancy concentration (see Section 4.3) due to rapid solidification and due to extended solubility decreasing greatly the mobility of the atoms with increasing distance from the chill block. Together with impurities at the wheel on-side picked up from the rotating chill block, a lower diffusivity might also have underlaid the higher pitting potential frequently observed for the wheel-off compared to the wheel-on side of the ribbons. Further at low anodic polarization the higher

current densities of the wheel-off side might stem from increased volume fraction of products of microsegregation compared to the chill side of corresponding samples.

4.2. Formation of a protective surface

The absence of $Mg_{17}Al_{12}$ precipitates alone does not account for the entire improvement obtained by RSP. Fig. 13 shows the values of the pitting potential at which the anodic current density exceeds $1\,mA\,cm^{-2}$ for homogeneous Mg–Al solid solutions as a function of aluminium concentration. The pitting potential increases steeply with increasing aluminium content above ~ 10 at %, i.e. in the range where extended solid solutions of aluminium in magnesium can be obtained by rapid solidication, reaching a plateau in pitting potential above ~ 30 at % Al. The interpolation between the values for β-Al_8Mg_5 and pure aluminium is based on the work by Mazurkiewicz [14] who found that Al_8Mg_5 behaves in even more aggressive pH = 6.2/1 M NaCl deaerated aqueous solution essentially like pure aluminium after depletion with magnesium from the Al_8Mg_5 surface. The relationship in Fig. 13, the increase in selectivity and the virtual cessation of macroscopic aluminium dissolution for rapidly solidified Mg–23.4 wt % Al ribbon altogether give evidence for the formation of an aluminium-enriched protective surface layer by depletion with magnesium. There has been considerable controversy in the literature whether selective dissolution leads to an homogeneous interdiffusion zone and, moreover, it is as yet totally unexplored whether a depleted, most often sponge-like surface zone gives rise to an even more protective layer under conditions allowing for oxidation and passivation of the remaining surface components. A magnesium dealloyed surface layer has been found after selective dissolution of magnesium from Mg–Cd alloys with 50 to 93 at % Cd leading to a porous crystalline layer of metallic cadmium becoming protective for alloys with ⩾ 93 at % Cd [15]. As for Fig. 13, a monotonic increase in pitting potential was also found in the concentration range between 10 and 35 to 45 at % Au for homogeneous Cu–Au and Ag–Au solid solutions when exposed to electrolytes in which pure gold forms a self-healing passive oxide surface film, while alloys with even higher gold concentrations showed the same breakthrough potential as does pure gold [16–18]. More recent work has shown that selective dissolution in low-melting In–Sn alloy generates a homogeneous interdiffusion zone of thickness ⩽ 50 μm [19], while in high-melting alloys such as Cu–Pd the depleted surface zone consists of microscopic tunnels [20] (compare also with [21]) into which the passivating oxide (as for Ag–Au alloys [22]) grows. The high mobility of the atoms in the present Mg–Al alloys investigated as evident from very low activation energies for transformation of the extended solid solution of 23.4 wt % Al in Mg [10] (~ 90 kJ mol^{-1}, i.e. ~ 45 kJ mol^{-1} lower than for the value obtained by linear interpolation of the values for tracer diffusion of the pure components [23]) together with the increased microstructural refinement by rapid solidification indicates the formation of

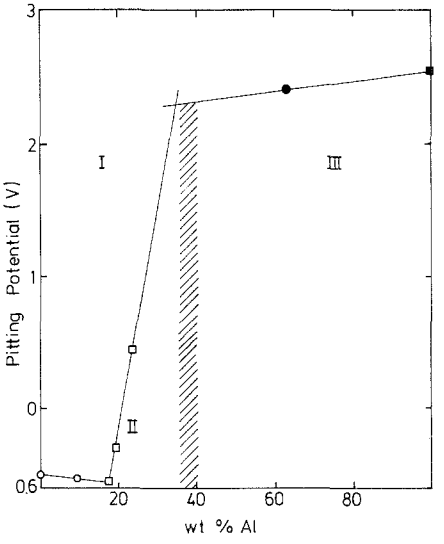

Figure 13 Pitting potential at a current density of $1\,mA\,cm^{-2}$ for homogeneous solid solutions in the system Mg–Al in aerated pH = 4.9 ± 0.1/0.001 M NaCl aqueous solution using a sweep rate of $6\,mV\,sec^{-1}$. (○, □) Rapidly solidified materials, (●, ■) chill-cast material. The breakthrough potential of pure aluminium (■) was estimated by using the values given by Kaiser [11]. Area I represents fast selective corrosion (pitting), area II slow selective corrosion controlled by vacancy-enhanced bulk-diffusion, and area III virtual passivity as a result of the corrosion characteristics of pure aluminium. The hatched area indicates the concentration above which initially homogeneous Mg–Al alloy solid solutions may behave as pure aluminium. (○) Piston-and-anvil splat, side of second impact of piston. (□) Free surface of melt-spun ribbon (see text).

a homogeneously depleted, aluminium-enriched underlayer increasing the stability of the oxide overlayer. The possible surface films (including pure alumina, mixed spinels such as $MgAl_2O_4$ [24] or a complex oxide–hydroxide (compare with [1]) in which aluminium is accumulated [25]) seem to be semi-permeable due to the relatively high current density observed during anodic polarization. This was not forthcoming from corresponding previous work [6–8].

4.3. Stability of the protective film

There was macroscopically no significant aluminium-dissolution in the early stages of corrosion, therefore the selective dissolution of magnesium from the ribbon containing 23.4 wt % Al appears to be related to volume diffusion rather than to other mechanisms suggested in the literature [18, 26, 27]. As found by Pickering and Wagner [28] and then by Pchelnikov *et al.* [29], selective dissolution by volume diffusion through a solid surface layer gives a linear relationship between current density, I, under potentiostatic conditions and $t^{1/2}$ (t = polarization time) in the very early stages of dealloying. The supply of the surface with atoms from the interior by one-dimensional, i.e. diffusion flux, j, perpendicular to the surface, is determined by [28]

$$j = \frac{x^0}{V}\left|\frac{D}{2(1 - x^0)t}\right|^{1/2} \qquad (2)$$

where x^0 is the initial molar fraction of the less noble component, V the molar volume of the alloy, D the interdiffusion coefficient, and t the time of potentiostatic electrolysis. When the supply of the surface with

magnesium atoms by diffusion from the bulk approximately equals the demand, i.e. the loss of material by electrochemical dissolution, then the overall current density observed, I_{ob}, approximately equals the current density equivalent of overall diffusion perpendicular to the surface, i_D

$$i_D = qFj \quad (3)$$

with q the valency and F Faraday's constant. By using a current density, I_{ob}, of $30\,\mu A\,cm^{-2}$ at the anodic plateau of Mg–23.4 wt % Al ribbon (Fig. 4), $x^0_{Mg} = 0.784$ and $V = 13.12\,cm^2\,mol^{-1}$, the interdiffusion coefficient in this material after 1 min anodic polarization, i.e., when having reached the anodic plateau, is indicated to be of the order of $\approx 2 \times 10^{-16}\,cm^2\,sec^{-1}$. This is eight orders of magnitude higher than for self-diffusivity of magnesium derived from radioactive tracer diffusion [23]. Pickering and Wagner [28] have found the zinc depletion of brass, for example, to be controlled by volume diffusion via divacancies rather than monovacancies, the corresponding diffusion coefficient of divacancies in copper ($1.3 \times 10^{-12}\,cm^2\,sec^{-1}$) being seven orders of magnitude higher than for monovacancies in copper ($3 \times 10^{-19}\,cm^2\,sec^{-1}$), the latter being equal to the self-diffusion coefficient of copper in copper. Two major problems can cause over-estimation of D from such depletions experiments:

1. surface roughening due to depletion of e.g. magnesium and/or due to the morphology of the ribbon undermining the assumption of one-dimensional diffusion to the surface; and

2. differential aeration cells caused by insufficient adherence of the coating at the exposed surface/coating junction of the ribbon and differential aeration cells at the electrolyte/air interface at the uncoated surface of the ribbon, so undermining the condition of uniform magnesium depletion from the surface.

Despite these possible inaccuracies, however, Fig. 9 shows that the decrease in I after 2 to 6 and 12 to 18 min of dissolution is consistent with the $I = fn(t)^{-1/2}$ relationship of Equation 3 and so indicating a high degree of homogeneity in the depletion zone. Using the relationship [28]

$$\delta = [2(1 - \phi^0_{Mg})Dt]^{1/2} \quad (cm) \quad (4)$$

where δ is the depth of depleted surface zone, ϕ^0_{Mg} the molar fraction of magnesium at the surface, i.e. ≈ 0 when depletion has occurred, D the interdiffusion coefficient and t the time of selective electrochemical attack, the thickness of the corresponding depleted zone amounts to 15 nm after 60 sec and ~ 3 nm after 4 min, i.e. when the dissolution of magnesium virtually stopped (Fig. 10a). For comparison, the width of the depleted zone of zinc-depleted brass was considered to amount to ~ 50 nm after 1000 sec (or 25 nm after 4 min) [28], while the dissolution of copper from homogeneous Cu–Au solid solution with 30 at % Cu was observed to continue for more than 1 h without stopping [30]. Evidently, a relatively low growth rate of the depletion zone (compared with brass) and the relatively rapid formation of a protective surface for Mg–Al compared with Cu–Au indicate competition between the anodic dissolution of magnesium and the passivation of aluminium and other species involved and a high field gradient through the (growing) oxide. This is also indicated by the serrated shape of the I-curve in Fig. 9 between 4 and 10 min of electrolysis. The second anodic peak after ~ 10 min of electrolysis (Fig. 9) may be accounted for by a decreased supply to the surface of atoms from the interior according to the $(t)^{-1/2}$ relationship (Equation 3) which interferes with the dynamic equilibrium between bulk alloy and electrolyte and so increases the instability of the aluminium-enriched surface layer. Note that a smooth metallic depletion zone was considered to become destabilized by penetration of the electrolyte [31]. Again, however, the $I = fn(t)^{-1/2}$ relationship becomes effective beyond the second peak indicating that the surface layer has some self-healing capacity as indicated by the ribbon surface that did not lose its metallic lustre during these observations. This self-healing ability seems to decrease with decreasing aluminium-content as the susceptibility to rapid magnesium-dissolution of the Mg–16.0 wt % Al splat sample shows (Fig. 12). The aluminium-enrichment of the surface of RS–Mg–Al-base alloys might, however, be one reason for the improved corrosion behaviour of PM–Mg–Al–Zn–Y alloys reported by Allied Signal in conjunction with other factors such as cathodic protection by the precipitation of $Mg_{25}Y_4$ or a variant (compare with [9]) and deserves further exploration.

5. Conclusions

1. Polarization studies indicate that sufficiently rapid solidification decreases the corrosion potential and decreases (by up to two orders of magnitude) the corrosion current of Mg–9.6 to 23.4 wt % Al in aerated 0.001 M NaCl aqueous solution. This decrease in corrosion current is attributed to the formation of a single-phase extended solid solution in the case of the rapidly solidified material eliminating the micro-galvanically active intercellular second phase present in the chill-cast material.

2. The effect of increasing aluminium content in solid solution for the rapidly solidified condition is to develop an anodic plateau at $\sim 30\,\mu A\,cm^{-2}$ and a steep increase in pitting potential between 10 and 23 wt % Al attributable to magnesium depletion from the alloy surface and the formation of a protective film. The increase in pitting potential (anodic polarization) indicates that a completely passive film would form in an extended solid solution at an aluminium concentration of ~ 30 wt %.

3. Chemical analysis of the electrolyte as a function of time of dissolution indicated for the rapidly solidified material that initially only magnesium was dissolved and this dissolution of magnesium ceased within 2 to 5 min. This behaviour is interpreted in terms of aluminium enrichment of the alloy surface giving rise to conditions that stabilize the formation of a passive alumina-based film.

4. Corresponding results for chill-cast material failed to show evidence for the formation of a protective film undoubtedly due to the presence of a coarse network of galvanically active $Mg_{17}Al_{12}$ within the magnesium-rich alloy matrix at the surface.

5. Modelling the observation of an anodic plateau in current density at $\sim 30\,\mu A\,cm^{-2}$ for rapidly solidified material in terms of dynamic equilibrium between demand and supply of magnesium undergoing anodic dissolution requires an interdiffusion coefficient of magnesium in the solid solution which is eight orders of magnitude higher than the self-diffusivity of magnesium.

Acknowledgements

The experiments were carried out at the University of Sheffield with financial support from Lockheed Missiles, Electronics and Space Group, Palo Alto, California, USA. The authors also acknowledge the supply by Allied Signal, Morristown, New Jersey, USA of samples of two rapidly solidified magnesium alloys consolidated by extrusion. We thank A. Joshi, H. Kaiser and R. Kirchheim for useful discussions.

References

1. M. R. BOTHWELL, in "The Corrosion of the Light Metals", edited by R. T. Foley *et al.* (Wiley, New York, 1967) p. 259.
2. E. F. EMLEY, in "Principles of Magnesium Technology" (Pergamon, Oxford, 1966) p. 670.
3. R. S. BUSK, in "Magnesium Products Design" (Marcel Dekker, New York, 1987) p. 498.
4. M. POURBAIX, in "Atlas of Electrochemical Equilibria in Aqueous Solutions" (Pergamon, Oxford, 1966) p. 139.
5. R. E. LEWIS, A. JOSHI and H. JONES, in "Processing of Structural Metals by Rapid Solidification", edited by F. H. Froes and S. J. Savage (American Society for Metals, Metals Park, Ohio, 1987) p. 367.
6. S. K. DAS and C. F. CHANG, in "Rapidly Solidified Crystalline Alloys", edited by S. K. Das (The Metallurgical Society of AIME, Warrendale, Pennsylvania, 1985) p. 137.
7. C. F. CHANG, S. K. DAS and D. RAYBOULD, in "Rapidly Solidified Materials", edited by P. W. Lee and R. S. Carbonara (American Society for Metals, Metals Park, Ohio, 1986) p. 129.
8. S. K. DAS, C. F. CHANG and D. RAYBOULD, *Light Metal Age* December (1986) 5.
9. F. HEHMANN, R. G. J. EDYVEAN, H. JONES and F. SOMMER, Conference Proceedings PM Aerospace Materials '87, edited by B. Williams and G. Dowson (Metal Powder Report Publishing Services, Shrewsbury, UK, 1988) pp. 46–1.
10. F. HEHMANN, "Rasch Erstarrh magnesium Mischkoistalle und ihr Umwandlungs – und korrosionsver-halten", Fortschoitt – Berichte VDI, Reihe 5, Nr. 155 (VDI-Verlag, Düsseldorf, 1989).
11. H. KAISER, in "Korrosion der Metalle" (Advanced Course, edited by H. Kaesche, University of Erlangen, Nürnberg, West Germany, 1984) pp. 4–7.
12. S. AKAVIPAT, E. B. HALE, C. E. HABERMANN and P. L. HAGANS, *Mater. Sci. Engng* **69** (1985) 311.
13. N. D. TOMASHOV, in "Theory of Corrosion and Protection of Metals" (MacMillan, New York, 1966) p. 493.
14. B. MAZURKIEWICZ, *Corr. Sci.* **23** (1983) 687.
15. J. I. GARDIAZABAL and J. R. GALVELE, *J. Electrochem. Soc.* **127** (1980) 255.
16. H. GERISCHER and H. RICKERT, *Z. Metallkde* **46** (1955) p. 681.
17. R. P. TISCHER and H. GERISCHER, *Z. Electrochem.* **62** (1958) p. 50.
18. H. GERISCHER, *Korrosion* **14** (1962) 59.
19. H. KAISER, *Werkstoffe und Korrosion*, to be published.
20. B. KABIUS, Thesis, University of Erlangen (1987).
21. A. J. FORTY and G. ROWLANDS, *Phil. Mag. A* **43** (1981) 171.
22. P. DURKIN and A. J. FORTY, *ibid.* **45** (1981) 95.
23. R. C. WEAST, in "CRC Handbook of Chemistry and Physics", 66th Edn (CRC, Florida, 1986) p. 46.
24. F. H. WÖLBIER, *Diffusion Defect Data* **50** (1987) 170.
25. W. A. FERNANDO, in Naval Surface Weapons Center Report TR 85–88 (Dahlgren, Virginia, 1985) p. 19.
26. H. SUGAWARA and H. EBIKO, *Corros. Sci.* **7** (1967) 513.
27. H. KAISER, "Alloy Dissolution", in "Corrosion Mechanisms" (Dekker, New York, 1987) p. 85.
28. H. W. PICKERING and C. WAGNER, *J. Electrochem. Soc.* **114** (1967) 698.
29. A. P. PCHELNIKOV, L. I. KRASINSKAYA, A. D. SITNIKOV and V. V. LOSEV, *Elektrokhimiya* **11** (1975) 37.
30. H. W. PICKERING and P. J. BYRNE, *J. Electrochem. Soc.* **118** (1971) 209.
31. C. WAGNER, *ibid.* **103** (1956) 571.

Received 3 June
and accepted 13 September 1988